Journal of Materials Chemistry A

Accepted Manuscript

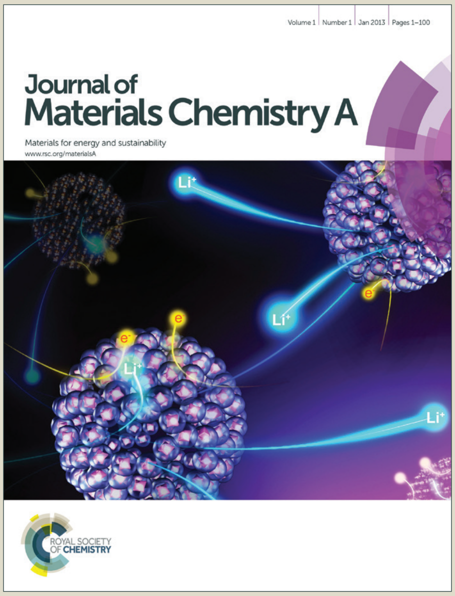

ROYAL SOCIETY OF CHEMISTRY

www.rsc.org/materialsA

Journal Name

ARTICLE

Received 00th January 20xx,
Accepted 00th January 20xx

DOI: 10.1039/x0xx00000x

www.rsc.org/

Mixed Matrix Membranes Comprising Two-Dimensional Metal-Organic Framework Nanosheets for Pre-Combustion CO_2 Capture: A Relationship Study of Filler Morphology versus Membrane Performance

Zixi Kang, Yongwu Peng, Zhigang Hu, Yuhong Qian, Chenglong Chi, Ling Yong Yeo, Lincoln Tee, and Dan Zhao*

A facile and scalable bottom-up method is used to synthesize a microporous jungle-gym-like metal-organic framework $[Cu_2(ndc)_2(dabco)]_n$ in the morphologies of nanocube and nanosheet. The obtained MOFs are blended with polybenzimidazole yielding a series of mixed matrix membranes (MMMs), which are evaluated for their performance in pre-combustion CO_2 capture (H_2/CO_2 separation). Pure gas permeation tests indicate that MMMs with partially oriented nanosheet MOFs possess the largest improvement compared with the neat polymer, with the overall H_2/CO_2 separation performance exceeding the 2008 polymer upper bound.

Introduction

The escalating anthropogenic carbon dioxide (CO_2) emission has aroused world-wide concerns nowadays for its side effects such as global warming,[1] ocean acidification,[2] and even nutrition deficiency in plants.[3] Three approaches have been proposed to capture CO_2 from power plants which are large point CO_2 sources: post-combustion CO_2 capture (CO_2/N_2 separation), pre-combustion CO_2 capture (CO_2/H_2 separation), and oxy-fuel (N_2/O_2 separation).[4-6] Compared to post-combustion approach, which captures dilute CO_2 (~15%) from flue gas at low pressures, the feed CO_2/H_2 mixed gas in pre-combustion approach is rich in CO_2 (up to 50%) and at higher pressures that facilitate CO_2 removal.[7] Among all the gas separation technologies, membrane-based one has the advantages of easy operation, facile scalability, and ready utilization of pressured feed gas source, thus receiving a lot of attention recently in pre-combustion CO_2 capture.[8-12] Although polymeric membranes have been utilized for this purpose, their performance is largely limited by the trade-off between permeability and selectivity depicted by the Robeson upper bounds.[13, 14] Inorganic membranes (e.g. zeolites, carbon molecule sieves, etc.) can offer a better balance between gas throughput and separation efficiency, but with weaker mechanical strength and higher costs.[15] Mixed matrix membranes (MMMs) were conceived by blending inorganic fillers into polymeric matrices hoping to combine the merits of polymeric membranes (e.g. flexibility, processability) and that of inorganic membranes (e.g. throughput, efficiency).[16-20] Most MMMs contain fillers of isotropic or near-isotropic morphologies, with size typically in the range of 100-1000 nm. It has long been suggested that MMMs comprising lamellar fillers with high-aspect-ratio and orientation perpendicular to gas concentration gradient would demonstrate excellent gas separation performance because of the increased tortuosity of gas permeation paths imposed by lamellar fillers.[21, 22] Accordingly, improved gas separation performance has been experimentally observed in MMMs containing oriented lamellar clays,[23] aluminophosphate,[24] titanosilicate,[25] zeolites,[26-29] etc.

As an emerging class of porous crystalline materials, metal-organic frameworks (MOFs) have received lots of attention in gas storage,[30, 31] gas separation,[32-35] heterogeneous catalysis,[36, 37] chemical sensing,[38, 39] etc. The last decade has witnessed booming interests of using MOFs as fillers to prepare MMMs for gas separation.[40-43] For example, Yang *et al.* reported MMMs composed of polybenzimidazole (PBI) as polymer matrix and ZIF-7 or ZIF-8 as fillers exhibiting excellent H_2/CO_2 separation performance.[44, 45] Bae *et al.* prepared high-performance MMMs made with 6FDA-DAM and ZIF-90 demonstrating great CO_2/CH_4 separation exceeding the Robeson upper bound.[46] Keskin *et al.* theoretically screened MOFs as fillers in MMMs for high efficiency natural gas purification.[47] Zhang *et al.* fabricated both flat and hollow fiber MMMs containing 6FDA-DAM and ZIF-8 showing significantly enhanced C_3H_6/C_3H_8 selectivity.[48, 49] In a recent study by Rodenas *et al.*, a CuBDC MOF was prepared in the morphology of freestanding nanosheets through a diffusion-mediated bottom-up strategy.[50] These MOF nanosheets were incorporated within a polyimide (PI) matrix with the preferred

---

Department of Chemical and Biomolecular Engineering, National University of Singapore, 4 Engineering Drive 4, 117585, Singapore
**E-mail: chezhao@nus.edu.sg*

orientation perpendicular to the gas flux, leading to a much higher CO_2/CH_4 separation selectivity than that of pristine polymeric membrane and MMMs containing bulk crystals of CuBDC MOF.

The above studies have revealed the great potential of MMMs containing MOFs as fillers, especially those with lamellar morphologies. However, a facile and economical way to synthesize lamellar MOFs still remains challenging.[51, 52] Generally speaking, there are two approaches to obtain lamellar MOFs: top-down and bottom-up. Top-down approaches refer to applying mechanical force such as ball-milling or sonication on bulk MOF crystals to yield exfoliated lamellar MOF sheets,[53-59] and bottom-up approaches indicate the direct synthesis of lamellar MOFs which include adjusting solvents,[60] contacting modes (e.g. layered synthesis),[50, 61] and modulated synthesis by using capping agents to facilitate the MOF crystal growth along 2D directions (e.g. epitaxial growth).[62, 63] In this study, we prepared one MOF $[Cu_2(ndc)_2(dabco)]_n$ (ndc = 1,4-naphthalene dicarboxylate, dabco = 1,4-diazabicyclo[2.2.2]octane)[64] with various morphologies (bulk crystal, nanocube, and nanosheet) using a modulated synthetic approach. These MOFs were blended with PBI affording a serious of MMMs. The performance of these MMMs in pre-combustion CO_2 capture (H_2/CO_2 separation) was systematically studied to reveal the relationship between filler morphology and membrane performance.

Experimental section

Materials and Methods

All chemicals and reagents are commercial available and were used without further purification. Polybenzimidazole (PBI) was kindly provided by PBI performance products, Ins. Powder X-ray diffraction (PXRD) patterns were obtained on a Bruker D8 Advance X-ray powder diffractometer equipped with a Cu sealed tube (λ = 1.54178 Å) at a scan rate of 0.02 deg s^{-1}. Scanning electron microscopy (SEM) was conducted on a JEOL-JEM5600 Lab-SEM (15 kV) equipped with an energy dispersive spectrometer. Samples were treated via Pt sputtering before observation.

Synthesis of MOFs with Different Morphologies

The synthesis of MOF $[Cu_2(ndc)_2(dabco)]_n$ in the morphologies of bulk crystal, nanocube, and nanosheet was carried out by revising reported procedures.[62, 63] The bulk crystal MOF was synthesized using a solvothermal method. First, a N,N-dimethylformamide (DMF) solution (20 ml) containing 1,4-naphthalenedicarboxylic acid (1,4-ndc, 70 mg) and 1,4-diazabicyclo[2.2.2]octane (dabco, 18 mg) was poured into a DMF solution (30 ml) containing $Cu(CH_3COO)_2{\cdot}H_2O$ (90 mg). The mixed solution was stirred for 30 min before being transferred into an autoclave and subsequently heated at 100 °C for 24 h. The precipitated product was filtered, washed with anhydrous ethanol for several times, and dried at 75 °C under vacuum overnight.

MOFs in the morphologies of nanocube and nanosheet were prepared using a reflux method that can be facilely scaled up. For a typical synthesis of nanocube MOF, $Cu(CH_3COO)_2{\cdot}H_2O$ (0.36 g) and acetic acid (1.04 ml) was dissolved in ethanol (30 ml) in a 100ml flask. An ethanol solution (20 ml) containing 1,4-ndc (0.28 g), dabco (0.072 g), and pyridine (1.52 ml) was poured into the previous solution. The mixed solution was stirred for 30 min before being heated under reflux (~100 °C) for 24 h. The precipitated product was filtered, washed with anhydrous ethanol for several times, and dried at 75 °C under vacuum overnight.

A similar reflux procedure was applied to the synthesis of nanosheet MOF. Briefly, $Cu(CH_3COO)_2{\cdot}H_2O$ (0.36 g) was dissolved in ethanol (30 ml) in a 100 ml flask. An ethanol solution (20 ml) containing 1,4-ndc (0.28 g), dabco (0.072 g), and pyridine (2.8 ml) was poured into the previous solution. The mixed solution was stirred for 30 min before being heated under reflux (~100 °C) for 24 h. The precipitated product was filtered, washed with anhydrous ethanol for several times, and dried at 75 °C under vacuum overnight.

Preparation of MMMs

All the MMMs in this study were prepared similarly. Taking NS@PBI-20 for example, PBI (~2g), which was previously heated at 180 °C under vacuum for at least 12 h to remove moisture and any adsorbed impurities, was dissolved in N-methyl-2-pyrrolidone (NMP, 60 ml) by stirring at 120 °C for 48 h, followed by filtration after cooling down to room temperature. Nanosheet MOF (60 mg) was suspended into a DMF solution (2 mL) through sonication, and was mixed with the previous PBI solution followed by sonication-stirring to give the membrane casting solution, which was casted onto a flat glass substrate and dried at 75 °C under vacuum for 12 h. After cooling down to room temperature, the membrane was peeled off and further dried at 200 °C under vacuum for 1 day to give the final MMM.

The thickness of obtained MMMs was measured by a micrometer caliper. The MOF loading of MMMs was calculated by the weight of MOFs divided by the total weight of MOFs plus polymer.

Gas Sorption Measurements

Gas sorption isotherms were measured up to 1 bar using a Micromeritics ASAP2020 surface area and pore size analyzer. Before measurements, the sample (~100 mg) was solvent-exchanged with methanol for 3 days and degassed under a reduced pressure (< 10^{-2} Pa) at 150 °C for 12 h. UHP grade He, N_2, H_2, and CO_2 were used for all the measurements. Oil-free vacuum pumps and oil-free pressure regulators were used to prevent contamination of samples during degassing process and isotherm measurement. The temperatures of 77 K, 273 K, and 298 K were maintained with a liquid nitrogen bath, an ice-water bath, and under room temperature, respectively. The Brunauer–Emmett–Teller (BET) surface areas were calculated from N_2 adsorption isotherms at 77 K. Pore size distribution data were also calculated from the N_2 adsorption isotherms at 77 K based on non-local density functional theory (NLDFT) model in the Micromeritics ASAP2020 software package (assuming slit pore geometry).

Single Gas Permeation Tests

The single gas (H_2 and CO_2) permeabilities of MMMs were carried out using a variable pressure constant-volume gas permeation cell technique. The gas permeation cell setup and testing procedures have been described previously.[65] Each membrane sample was solvent-exchanged with methanol for 3 days and dried under vacuum at 200 °C overnight to removal solvent molecules. Each test was performed after the sample was degassed to a pressure of 1-10 mTorr and the system reached thermal equilibrium after at least 5 h. The operating temperature was set at 35 °C unless otherwise indicated, and the upstream gas gauge pressure was set at 2, 3.5, and 5 bars, respectively. The gas permeability was calculated from the rate of pressure increasing (dp/dt) at a steady state according to equation 1:

$$P = \frac{273 \times 10^{10}}{760} \frac{VL}{AT(p_2 \times 76/14.7)} \left(\frac{dp}{dt} \right) \quad \text{(Equation 1)}$$

where P is the membrane gas permeability in Barrer (1 Barrer = $1 \times 10^{-10} cm^3(STP)cmcm^{-2}s^{-1} \cdot cmHg^{-1}$), V represents the volume of the downstream reservoir (cm^3), L refers to the membrane thickness (cm), A is the effective membrane area (cm^2), T is the operating temperature (K), and p_2 indicates the upstream pressure (psia).

The ideal selectivity (permselectivity) was calculated based on equation 2:

$$\alpha(i/j) = \frac{P_i}{P_j} \quad \text{(Equation 2)}$$

Calculation of Isosteric Heat of Adsorption (Q_{st})

The CO_2 adsorption isotherms measured at 273 K and 298 K were first fitted to a virial equation (Equation 3). The fitting parameters were then used to calculate the isosteric heat of adsorption (Q_{st}) using Equation 4,

$$\ln P = \ln N + \frac{1}{T} \sum_{i=0}^{m} a_i N^i + \sum_{i=0}^{n} b_i N^i \quad \text{(Equation 3)}$$

$$Q_{st} = -R \sum_{i=0}^{m} a_i N^i \quad \text{(Equation 4)}$$

where P is pressure (mmHg), N is adsorbed quantity (mmol g^{-1}), T is temperature (K), R is gas constant (8.314 J K^{-1} mol^{-1}), a_i and b_i are virial coefficients, m and n represent the number of coefficients required to adequately describe the isotherms (herein, m = 5, n = 2).

Calculation of Selectivity via Ideal Adsorption Solution Theory (IAST)

The H_2 and CO_2 adsorption isotherms were first fitted to a dual-site Langmuir-Freundlich (DSLF) model (Equation 5),

$$q = \frac{q_{sat,A} b_A p^{\alpha_A}}{1 + b_A p^{\alpha_A}} + \frac{q_{sat,B} b_B p^{\alpha_B}}{1 + b_B p^{\alpha_B}} \quad \text{(Equation 5)}$$

where q is the amount of adsorbed gas (mmol g^{-1}), p is the bulk gas phase pressure (bar), q_{sat} is the saturation amount (mmol g^{-1}), b is the Langmuir-Freundlich parameter ($bar^{-\alpha}$), α is the Langmuir-Freundlich exponent (dimensionless) for two adsorption sites A and B indicating the presence of weak and strong adsorption sites.

IAST starts from the Raoults' Law type of relationship between fluid and adsorbed phase,

$$P_i = P y_i = P_i^o x_i \quad \text{(Equation 6)}$$

$$\sum_{i=1}^{n} x_i = \sum_{i=1}^{n} \frac{P_i}{P_i^0} = 1 \quad \text{(Equation 7)}$$

where P_i is partial pressure of component i (bar), P is total pressure (bar), y_i and x_i represent mole fractions of component i in gas and adsorbed phase (dimensionless). P_i^0 is equilibrium vapour pressure (bar).

In IAST, P_i^0 is defined by relating to spreading pressure π,

$$\frac{\pi S}{RT} = \int_0^{P_i^0} \frac{q_i(P_i)}{P_i} dP_i = \Pi \text{ (Constant)} \quad \text{(Equation 8)}$$

where π is spreading pressure, S is specific surface area of adsorbent (m^2 g^{-1}), R is gas constant (8.314 J K^{-1} mol^{-1}), T is temperature (K), $q_i(P_i)$ is the single component equilibrium obtained from isotherm (mmol g^{-1}).

For a DSLF model, we have an analytical expression for the integral,

$$\int_0^{P_i^0} \frac{q_i(P_i)}{P_i} dP_i = \Pi \text{ (Constant)} =$$

$$\frac{q_{sat,A}}{\alpha_A} \ln[1 + b_A (P_i^0)^{\alpha_A}] + \frac{q_{sat,B}}{\alpha_B} \ln[1 + b_B (P_i^0)^{\alpha_B}] \quad \text{(Equation 9)}$$

The isotherm parameters are derived from the previous fitting. For a binary component system the unknowns will be Π, P_1^0, and P_2^0 which can be obtained by simultaneously solving Equations 7 and 9.

The adsorbed amount for each compound in a mixture is

$$q_i^{mix} = x_i q_T \quad \text{(Equation 10)}$$

$$\frac{1}{q_T} = \sum_{i=1}^{n} \frac{x_i}{q_i(P_i^o)} \quad \text{(Equation 11)}$$

where q_i^{mix} is the adsorbed amount of component i (mmol g^{-1}), q_T is the total adsorbed amount (mmol g^{-1}).

The adsorption selectivities S_{ads} were calculated using Equation 12.

$$S_{ads} = \frac{q_1 / q_2}{p_1 / p_2} \quad \text{(Equation 12)}$$

In this study, IAST calculations were carried out assuming a H_2/CO_2 binary mixed gas with a molar ratio of 50:50 at 298 K and pressures up to 1 bar.

Calculation of Apparent Activation Energy of Permeation (E_p)

The temperature dependence of gas permeation can be stated by Arrhenius equations,

$$P_i = A \exp(-\frac{E_p}{R \cdot T_i}) \quad \text{(Equation 13)}$$

$$\ln(P_i) = a - \frac{E_p}{R} \cdot \frac{1}{T_i} \quad \text{(Equation 14)}$$

$$\ln(\frac{P_{308K}}{P_{333K}}) = \frac{E_p}{R} (\frac{1}{333} - \frac{1}{308}) \quad \text{(Equation 15)}$$

where P_i is permeability of one gas at different temperatures, A represents the pre-exponential factor of this gas, E_p is the apparent activation energy of permeation for this gas, R is gas constant (8.314 J K^{-1} mol^{-1}), T is temperature (K).

Results and discussion

Morphology of MOFs

The MOF $[Cu_2(ndc)_2(dabco)]_n$ was chosen because of its narrow undulating channels with pore sizes of 5.4 Å × 6.2 Å viewed along [100] direction and 3.7 Å × 3.7 Å viewed along [001] direction (Fig. 1a). Such small pore sizes would make it appealing for gas separation as they are close to the dynamic diameters of the gas molecules to be separated (H_2: 2.89 Å, CO_2: 3.3 Å). In addition, the partial rotating of naphthalene moieties would further narrow down the pore opening making it possible for gas separation based on molecule sieving mechanism.[66-68] $[Cu_2(ndc)_2(dabco)]_n$ in the morphology of nanosheet was synthesized by revising a reported method using pyridine as a capping agent to impede the crystal growth along [001] direction.[62, 63] Briefly, a reflux of an ethanol solution containing ligands, metal salt, and capping agent for 24 h could afford the target MOF nanosheet in good yield (see Experimental Section). Compared with the reported method, out synthesis of MOF nanosheet is easy to operate and can be facilely scaled up, thus paving a solid way towards the large scale application of these fillers.

The prepared MOF materials in the morphologies of bulk crystal (BC), nanocube (NC), and nanosheet (NS) were checked by field-emission scanning electron microscopy (FE-SEM). As can be seen from FE-SEM images (Fig. 2), the crystal size of BC MOF can be up to 10 µm, but is reduced to 30-50 nm in NC MOF indicating the effectiveness of modulated synthesis. NS MOF has a flake size of ~100 nm with a thickness of ~10 nm, leading to an aspect ratio of ~10 confirming its lamellar morphology (Fig. 2f). Powder X-ray diffraction (PXRD) patterns reveal that MOFs with different morphologies all maintain the same reported crystal structure (Fig. 1b). In order to check the possible orientation of NS MOF on a flat surface, a suspension of NS MOF in ethanol was filtered onto a nanoporous anodic alumina oxide (AAO) support. The obtained sample exhibited a stronger X-ray diffraction signal from (001) plane than (100) plane, confirming the preferred exposure of (001) plane due to an oriented stacking.

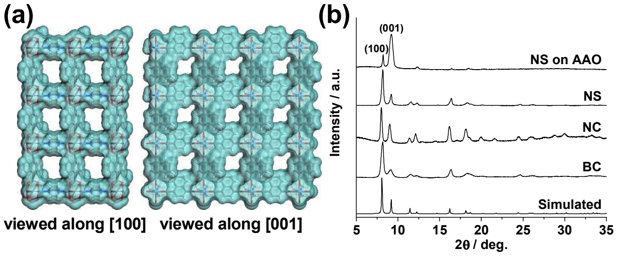

Fig. 1 (a) Pore size of the MOF $[Cu_2(ndc)_2(dabco)]_n$ viewed along [100] direction (5.4 Å × 6.2 Å) and [001] direction (3.7 Å × 3.7 Å); (b) PXRD patterns of simulated MOF, MOF with various morphologies (BC: bulk crystal; NC: nanocube; NS: nanosheet), and nanosheet MOF deposited onto AAO support with oriented stacking.

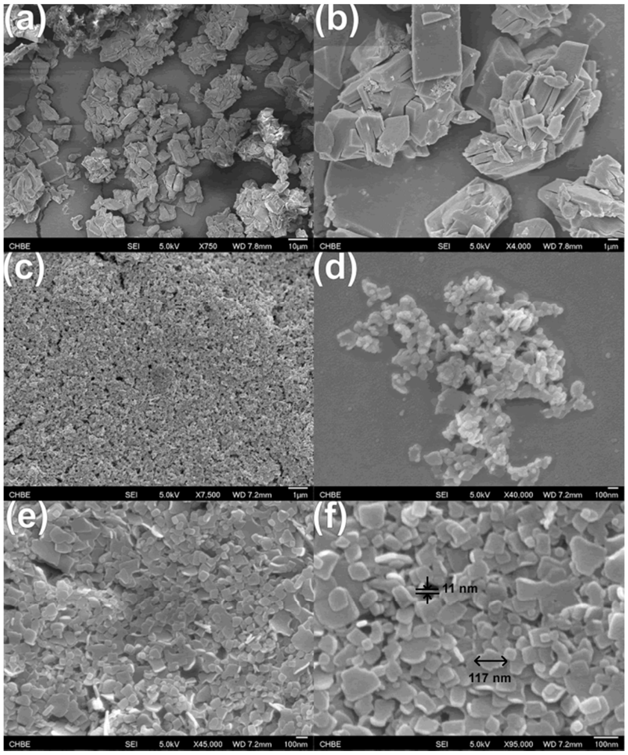

Fig. 2 FE-SEM images of the MOF $[Cu_2(ndc)_2(dabco)]_n$ with various morphologies: (a, b) bulk crystal; (c, d) nanocube; (e, f) nanosheet.

Porosity and Gas Uptakes of MOFs

The permanent porosity and pore size distribution of BC, NC, and NS MOFs were evaluated by N_2 sorption isotherms collected at 77 K under pressures up to 1 atm (Fig. 3a). All the three samples exhibit hybrid Type I/IV isotherms based on the IUPAC definition.[69] Type I isotherms are featured by the sharp increase of gas uptake at low pressures confirming the microporous structures (pore size < 2 nm) of these MOFs that agree well with the crystal structure. Type IV isotherms are highlighted by the hysteresis between adsorption and desorption branches coming from mesoporous structures (pore size between 2 and 50 nm) possibly due to interstitial voids of crystal particles in this study.[70] The Brunauer, Emmett, and Teller (BET) surface areas of NC MOF and NS MOF are 808 and 945 m^2 g^{-1}, respectively, which are higher than that of BC MOF (564 m^2 g^{-1}) and is in agreement with the previous report.[62, 63] The difference of BET surface area among three MOFs may originate from the slightly different crystallinity caused by various synthetic conditions.[70] Pore size distribution data were calculated by applying the nonlocal density functional theory (NLDFT) to the adsorption data assuming slit pore geometry. All the three MOFs exhibit microporous size distribution at 5.8-6.9 Å that is close to the value directly measured from the crystal structure.

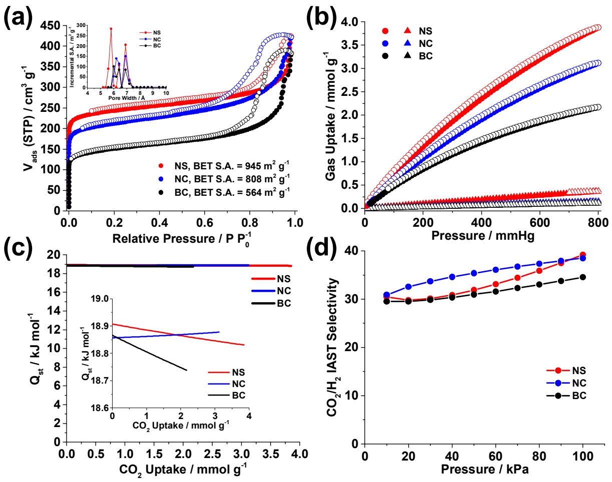

Fig. 3 (a) N_2 sorption isotherms of MOF with various morphologies measured at 77 K (closed, adsorption; open, desorption) as well as the pore size distribution calculated from NLDFT assuming slit pore geometry (imbedded); (b) CO_2 (circle) and H_2 (triangle) sorption isotherms of MOF with various morphologies measured at 273 K; (c) CO_2 isosteric heat of adsorption (Q_{st}) of MOF with various morphologies (imbedded: magnified view); (d) CO_2/H_2 IAST selectivity of MOF with various morphologies calculated at 298 K.

H_2 and CO_2 sorption isotherms were collected to evaluate the selective gas sorption properties of these MOFs. As can be seen in Fig. 3b, NS MOF has the highest CO_2 uptake capacity at 273 K under 1 bar (3.76 mmol g^{-1}), which is much higher than that of some other MOFs having similar surface areas.[33] NC MOF has a medium CO_2 uptake capacity under a similar condition (3.02 mmol g^{-1}), while BC MOF has the least one (2.11 mmol g^{-1}). The zero-coverage isosteric heat of adsorption (Q_{st}) calculated for BC, NC, and NS MOFs are 18.86, 18.85, and 18.90 kJ mol^{-1}, respectively (Fig. 3c), which are quite close to each other indicating similar interactions with CO_2. Therefore, the different CO_2 uptake capacity among the three MOFs can be attributed to the difference of surface area. It is worth noting that the Q_{st} of CO_2 for three MOFs remains relatively constant over the full CO_2 loading range suggesting homogeneous sorption sites for CO_2 provided by the narrow MOF channels, which also account for the high CO_2 uptake capacities. Compared to CO_2, H_2 has much weaker interactions with MOFs leading to greatly reduced uptake capacities under similar conditions (Fig. 3b). The single gas isotherms of CO_2 and H_2 were used to calculate the binary CO_2/H_2 adsorption selectivity via ideal adsorbed solution theory (IAST) taking into consideration the competitive sorption between each component.[71, 72] The IAST CO_2/H_2 selectivities of BC, NC, and NS MOFs vary between 29 and 39 at 298 K with pressures up to 1 atm, proving their suitability for CO_2/H_2 separation (Fig. 3d).

Characterization of MMMs

The successful synthesis of a microporous MOF with different morphologies and selective CO_2 uptake properties prompts us to check the performance of these materials being used as fillers in MMMs for pre-combustion CO_2 capture. Polybenzimidazole (PBI) was chosen as the polymer matrix because of its high thermal stability (stable up to 500 °C) and good processability which represents the state of the art H_2-selective polymeric membrane for pre-combustion CO_2 capture.[73] MMMs containing BC, NC, and NS MOFs with 20 wt% loading content each were prepared according to a published procedure.[44] In a typical process for MMM preparation, MOFs were firstly dispersed in DMF by stirring and sonication, followed by the addition of PBI dissolved in N-methyl-2-pyrrolidone (NMP). The well-mixed solutions were then cast onto silica wafers and dried in a vacuum oven affording MMMs named as BC@PBI-20, NC@PBI-20, and NS@PBI-20, respectively, depending on the MOF fillers being used. Before gas permeation test, a solvent exchange process was carried out for MMMs to fully activate the porous MOF fillers. This process was found to be important to enhance the gas separation performance of the resultant MMMs.[44]

One of the key issues of MMMs is to ensure good compatibilities between fillers and polymer matrices to avoid possible structural defects such as sieve-in-a-cage and pinholes which are detrimental to gas separation performance.[74, 75] Compared to inorganic fillers such as zeolites, the organic-inorganic hybrid chemical structure of MOFs could grant them much better compatibilities with polymer matrices.[76] This is confirmed in the cross-sectional FE-SEM images of our MMMs, which reveal no structural defects indicating a good compatibility between MOF fillers and polymer matrix (Fig. 4a-c). In addition, plastic deformation featured by polymer veins was observed in our MMMs, which has been reported previously in MOF-containing MMMs and was attributed to the strong interactions between MOF fillers and polymer matrices.[76] Thanks to the well-dispersed MOF fillers and strong interactions with polymer matrices, the resultant MMMs exhibit good mechanical strength and flexibility similar to that of pure PBI membrane (Fig. 4d).

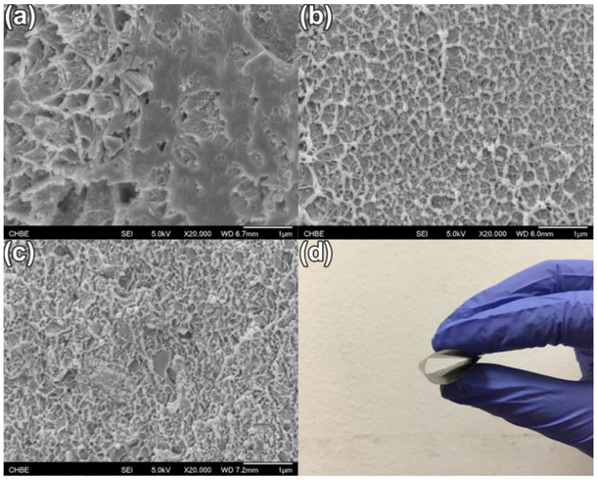

Fig. 4 FE-SEM cross-sectional images of (a) BC@PBI-20, (b) NC@PBI-20, and (c) NS@PBI-20, along with (d) optical image of NS@PBI-20 demonstrating its flexibility.

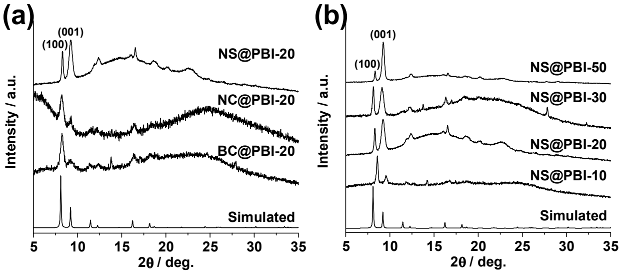

Fig. 5 (a) PXRD patterns of simulated MOF and MMMs containing 20 wt% of MOFs with various morphologies; (b) PXRD patterns of simulated MOF and MMMs containing nanosheet MOF with various loading amounts.

PXRD patterns of MMMs revealed the crystalline integrity of MOF fillers being incorporated into the PBI matrix (Fig. 5a). For the sample of NS@PBI-20, it is interesting to note that the peak intensity from (001) plane is relatively stronger than that of (100) plane, suggesting a partially oriented stacking of MOF fillers with more exposure of (001) planes toward the upstream face of MMMs. Such an oriented stacking may arise from the shear force or surface tension imposed on the lamellar MOF fillers during membrane fabrication,[16, 50] and is beneficial for gas separation because (001) plane has a smaller pore size which helps to differentiate gases based on their size difference. In order to confirm the oriented stacking of NS MOF, MMMs with other loading amounts of NS were prepared (10, 30, and 50 wt%, denoted as NS@PBI-10, NS@PBI-30, and NS@PBI-50, respectively). It can be clearly identified from the PXRD patterns that the peak intensity ratio of (001) plane over (100) plane is rising upon increasing NS loading, demonstrating a higher degree of oriented stacking at higher NS MOF loadings (Fig. 5b). The intensified oriented stacking of NS MOF in MMMs with higher MOF loadings was further confirmed by FE-SEM images, where lamellar structure is cleared identified in NS@PBI-50 (Fig. 6).

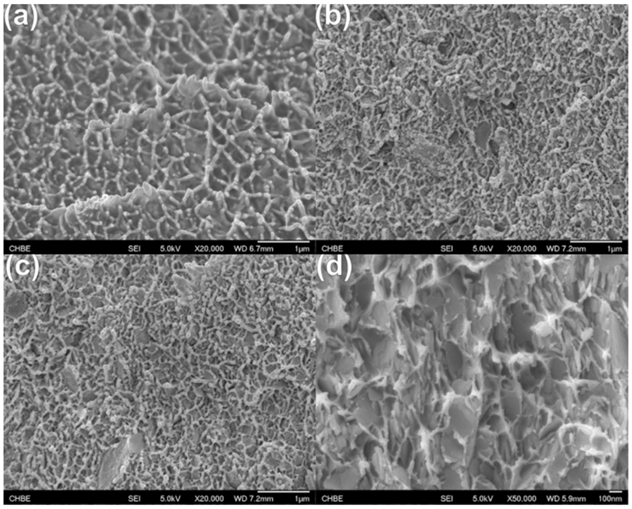

Fig. 6 FE-SEM cross-sectional images of (a) NS@PBI-10, (b) NS@PBI-20, (c) NS@PBI-30, and (d) NS@PBI-50.

Gas Separation Performance of MMMs

Our MMMs containing MOF fillers with various morphologies serve as a perfect platform to study the relationship between filler morphology and membrane performance in pre-combustion CO_2 capture. Single H_2 and CO_2 gas permeabilities were obtained based on a time lag method, which measures pressure increase in a constant downstream volume as a function of time to determine gas permeability.[77] Each test was performed after the sample was degassed to a pressure of 1-10 mTorr, and the system reached thermal equilibrium after at least 5 h. Feed pressures were varied among 2, 3.5, and 5 bars, and testing temperature was set at 35 °C unless otherwise indicated. Each membrane was tested 3-5 times for each gas, and the average values were recorded (Table 1). Ideal selectivities (permselectivities) were calculated using the averaged H_2 and CO_2 permeabilities, and were plotted versus H_2 permeabilities in Fig. 7 containing 2008 Robeson upper bound for H_2/CO_2 separation to reflect state of the art polymeric membrane performance.[14]

Table 1 Gas permeation data of pure PBI membrane and MMMs containing MOFs

Membrane	T^a	P^b	Perm^c_{H2}	Perm^c_{CO2}	$\alpha_{H2/CO2}$
PBI	35	2.0	3.62±0.02	0.40±0.01	9.05
		3.5	3.62±0.02	0.39±0.02	9.28
		5.0	3.61±0.01	0.38±0.02	9.50
BC@PBI-20	35	2.0	5.23±0.04	0.48±0.01	10.9
		3.5	5.18±0.04	0.41±0.01	12.6
		5.0	5.15±0.05	0.37±0.01	13.9
NC@PBI-20	35	2.0	5.29±0.09	0.36±0.01	14.7
		3.5	5.29±0.01	0.30±0.01	17.6
		5.0	5.29±0.07	0.24±0.01	22.0
NS@PBI-10	35	2.0	4.84±0.02	0.35±0.01	13.8
		3.5	4.86±0.03	0.26±0.01	18.7
		5.0	4.85±0.02	0.23±0.01	21.1
NS@PBI-20	35	2.0	6.14±0.01	0.39±0.02	15.7
		3.5	6.15±0.02	0.27±0.01	22.8
		5.0	6.13±0.03	0.23±0.01	26.7
NS@PBI-30	35	2.0	12.1±0.1	1.11±0.01	10.9
		3.5	11.9±0.2	0.97±0.01	12.3
		5.0	11.7±0.3	0.85±0.01	13.8
NS@PBI-50	35	2.0	69.1±0.5	15.1±0.1	4.6
		3.5	66.4±0.3	13.8±0.1	4.8
		5.0	63.2±1.8	12.9±0.1	4.9
NS@PBI-20	60	2.0	10.4±0.01	0.88±0.01	11.8
		3.5	10.3±0.02	0.72±0.01	14.3
		5.0	10.4±0.02	0.70±0.01	14.9

[a] Temperature (°C); [b] pressure (bars); [c] permeability (Barrers)

Pure PBI membrane has a H_2 permeability of 3.05±0.02 Barrers and a H_2/CO_2 permselectivity of 9.24 at 35 °C under a feed pressure of 2 bars, which is within the same range of the reported values.[73] It is widely accepted that gas separation performance of polymeric membranes follows the solution-diffusion mechanism, where gas permeability **P** can be expressed by the product of solubility **S** and diffusivity **D**: **P** = **S** × **D**.[78] The significantly lower critical temperature of H_2 (33 K) implies its small solubility in polymeric membranes; therefore H_2-selective membranes are operated based on the larger diffusivity of H_2 within polymer voids due to its smaller molecular size.

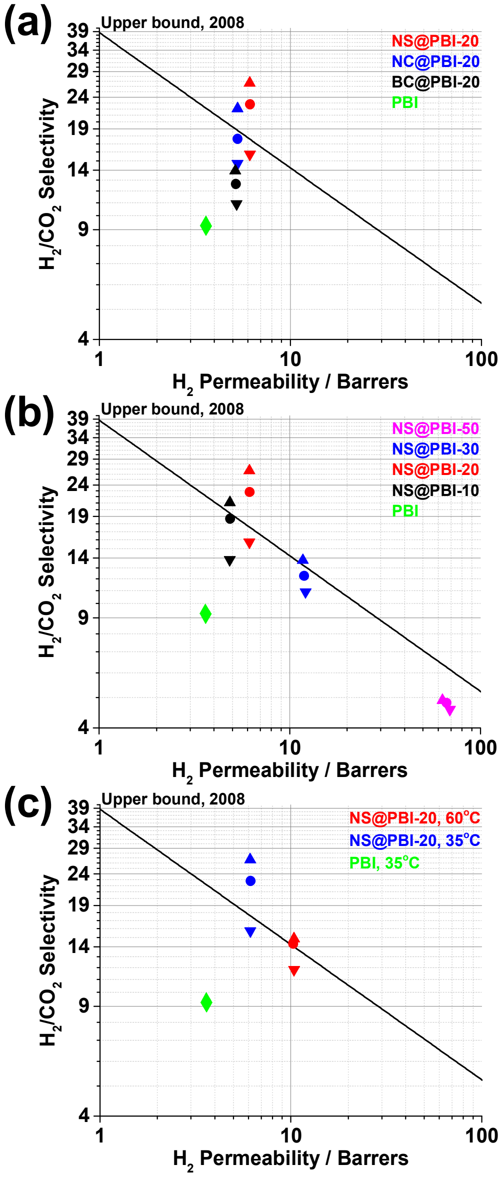

Fig. 7 H_2 permeabilities versus H_2/CO_2 selectivities of pure PBI membranes and (a) MMMs containing 20 wt% of MOFs with various morphologies, (b) MMMs containing nanosheet MOF fillers with various loading amounts, and (c) NS@PBI-20 measured under 35 and 60 °C, respectively. Down-triangle: 2 bars; circle: 3.5 bars; up-triangle: 5 bars. Error bars are too small to be displayable. The 2008 Robeson upper bound for H_2/CO_2 separation is included to reflect state of the art polymeric membrane performance.

Increasing the feed pressure led to decreased H_2 and CO_2 permeabilities, which can be attributed to saturation of the Langmuir sites based on dual sorption theory.[79] Compared to H_2, CO_2 is more condensable in the polymer voids causing a sharper decrease of permeability along with pressure. As a result, the H_2/CO_2 permselectivity increased under higher pressures (Fig. 7a). It needs to be pointed out that CO_2 permeability may increase dramatically under even higher pressures due to CO_2-induced plasticization.[80] This phenomenon was not observed in our study because of the adopted medium pressure range that is below the plasticization pressure of CO_2.

Adding porous MOF fillers into polymeric membranes would normally increase gas permeability due to the introduction of extra voids from the MOF fillers. However, the gas selectivity may or may not improve depending on the specific interactions of each gas component with MOF fillers. It has been theoretically verified in PBI/ZIF-7 MMM that H_2 diffusion passes through both ZIF-7 and PBI phases and is not retarded by the addition of ZIF-7, but CO_2 is mostly trapped in ZIF-7 cages therefore CO_2 diffusion in PBI/ZIF-7 is inhibited by ZIF-7.[81] In our case, both H_2 permeability and H_2/CO_2 selectivity are improved in MMMs containing MOF bulk crystals (BC@PBI-20, Fig. 7a). The improved H_2/CO_2 selectivity comes from a smaller increase of CO_2 permeability in MMMs, possibly because of the impeded CO_2 diffusion in MOF fillers coming from narrow pore size and homogeneously strong interactions.[81] The increased H_2/CO_2 selectivity under higher pressures was also observed in MMMs, suggesting their improved separation performance under higher pressures that may be suitable for pre-combustion CO_2 capture.

Our hypothesis that the morphology of MOF fillers should have an impact on the membrane separation performance is verified by the parallel compare of MMMs containing the same loading amounts of MOF fillers but with different morphologies. In the reported MMMs containing MOFs, much effort has been devoted to reduce the MOF particle size for better compatibilities with the polymer matrices and to prevent the particle agglomeration and sedimentation.[82] This has been facilely achieved herein that MOFs with nanocube morphology and particle size of 30-50 nm were readily synthesized using the modulated synthetic approach (Fig. 2). Compared to MMMs with bulk MOF crystals (BC@PBI-20), MMMs containing nanocube MOFs (NC@PBI-20) exhibited comparable H_2 permeabilities but increased H_2/CO_2 selectivities (Fig. 7a), which can be attributed to a more uniform distribution of NC MOF fillers inside PBI matrix (Fig. 4). In addition, the difference of BET surface areas and CO_2 uptake capacities between NC and BC MOFs may also be relevant. It is worth noting that the H_2/CO_2 selectivity of NC@PBI-20 is increased to 22.0 under a feed pressure of 5 bars, which has exceeded the 2008 Robeson upper bound and is rarely reported in MOFs-containing MMMs for H_2/CO_2 separation.[43] As has been expected, MMMs containing lamellar MOF fillers (NS@PBI-20) exhibit the best gas separation performance among the MMMs series in this study. Compared to pure PBI membranes, H_2 permeability in NS@PBI-20 has doubled to

6.13 ± 0.03 Barrers at 5 bars, with a H_2/CO_2 permselectivity of 26.7 exceeding the 2008 Robeson upper bound and is also the highest among all the membranes in this study (Fig. 7a). Considering the similar BET surface areas and CO_2 uptake capacities between NS and NC MOFs, morphology difference of MOF fillers should be the dominating factor in determining the excellent gas separation performance of NS@PBI-20. As has been demonstrated previously, NS MOFs dispersed in PBI matrix exhibit a certain degree of oriented stacking with more exposure of (001) crystal planes toward the gas concentration gradient. Due to the small pore size of (001) crystal plane (3.7 Å × 3.7 Å), such oriented stacking is beneficial for H_2/CO_2 separation as H_2 molecules can easily permeate through due to their weak interactions with MOFs and small molecular size (2.89 Å). However, the permeation of CO_2 molecules may be partially retarded because of their slower diffusion within MOF channels and larger molecular size (3.3 Å) so that some of them may have to follow more tortuous paths from interlayer gallery of lamellar MOF sheets to permeate through, leading to only slightly increased (at 2 bars) and even reduced (at 3.5 and 5 bars) permeabilities compared to that of pristine polymer membranes (Table 1). The influence of loading amount is also investigated for NS@PBI. MMMs containing 10, 20, 30, and 50 wt% loadings of NS MOFs were prepared and their gas separation performance was evaluated (Fig. 7b). On the one hand, H_2 permeability at 2 bars is significantly increased under higher MOF loadings, and reaches the highest value of 69.1 ± 0.5 Barrers in NS@PBI-50. This is anticipated as higher MOF loadings lead to larger portion of voids in MMMs which facilitates H_2 diffusion. On the other hand, H_2/CO_2 selectivity at 5 bars is improved from 21.1 to 26.7 when the NS MOF loading amount increases from 10 to 20 wt%, but starts to decrease at higher MOF loadings down to 4.9 in NS@PBI-50 which is even lower than that of the pristine PBI membrane (12.6). The decreased H_2/CO_2 selectivity of MMMs at higher MOF loadings can be attributed to MOF particle intercalation leading to continuous MOF connections across the entire membrane. As a result, gases may simply diffuse across the membrane via low-selective MOF particle bridges leading to reduced H_2/CO_2 selectivities.

Given the high temperature working condition of pre-combustion CO_2 capture, gas permeation tests on NS@PBI-20 at a higher temperature of 60 °C were carried out to study the temperature effect (Fig. 7c). Both H_2 and CO_2 permeabilities were increased at 60 °C, indicating an activated diffusion process. By fitting the experimental data with Arrhenius equations, the apparent activation energies of permeation (E_p) for H_2 and CO_2 in NS@PBI-20 were calculated to be 18.03 and 37.96 kJ mol^{-1}, respectively. As what we have discussed previously, MOFs have a higher Q_{st} for CO_2 than H_2, resulting in stronger interactions with CO_2 and accordingly slower diffusion of CO_2 within MOFs. The E_p trend correlates well with Q_{st} of H_2 and CO_2 in MOFs,[31, 33] suggesting the import role played by gas diffusion in the process of permeation through MMMs. Despite the increased H_2 permeability, a decreased H_2/CO_2 selectivity was observed at 60 °C, which originates from a faster increase of CO_2 permeability possibly due to larger pore openings of MOF fillers and their reduced CO_2 uptake capacities at higher temperatures. Nevertheless, a H_2 permeability of 10.4 ± 0.2 Barrers and H_2/CO_2 selectivity of 14.9 measured at 5 bars and 60 °C still put NS@PBI-20 above the 2008 Robeson upper bound.

Conclusions

In conclusion, we have prepared a series of MMMs by blending PBI with a Cu MOF $[Cu_2(ndc)_2(dabco)]_n$ with three different morphologies: bulk crystal (BC), nanocube (NC), and nanosheet (NS). The gas separation performance of these MMMs in the application of pre-combustion CO_2 capture was evaluated by measuring the single gas permeation data of H_2 and CO_2 under various pressures (2, 3.5, and 5 bars) and temperatures (35 and 60 °C). As has been expected, the morphology of MOF fillers plays an important role in determining the gas separation performance of resultant MMMs. Reducing the crystal particle size of MOF fillers from BC to NC leads to better separation performance because of a more uniform distribution of MOF fillers. The membrane performance can be further improved by using lamellar NS MOF fillers because of their partially oriented stacking within MMMs that make them serve as CO_2 barriers leading to increased H_2/CO_2 selectivities. The best gas separation performance was achieved in NS@PBI-20 at 35 °C under 5 bars, which exhibits a H_2 permeability of 6.13 ± 0.03 Bareers and H_2/CO_2 selectivity of 26.7 that has exceeded the 2008 Robeson upper bound and is rarely reported in MOF-containing MMMs. Our work has clearly depicted the importance of using lamellar porous MOF fillers in preparing MMMs for increased gas separation performance, and should be helpful to the design of next-generation hybrid membrane materials in the applications of clean energy and environmental sustainability.

Acknowledgements

This work is supported by National University of Singapore (NUS Start-up Funding R-279-000-369-133, CENGas R-261-508-001-646) and Singapore Ministry of Education (MOE AcRF Tier 1 R-279-000-410-112, AcRF Tier 2 R-279-000-429-112). Z.K. acknowledges the financial support by Fundamental Research Funds for the Central Universities (14CX02150A).

Notes and references

1. J. D. Shakun, P. U. Clark, F. He, S. A. Marcott, A. C. Mix, Z. Y. Liu, B. Otto-Bliesner, A. Schmittner and E. Bard, *Nature*, 2012, **484**, 49-54.
2. B. Hönisch, A. Ridgwell, D. N. Schmidt, E. Thomas, S. J. Gibbs, A. Sluijs, R. Zeebe, L. Kump, R. C. Martindale, S. E. Greene, W. Kiessling, J. Ries, J. C. Zachos, D. L. Royer, S. Barker, T. M. Marchitto, R. Moyer, C. Pelejero, P. Ziveri, G. L. Foster and B. Williams, *Science*, 2012, **335**, 1058-1063.
3. S. S. Myers, A. Zanobetti, I. Kloog, P. Huybers, A. D. B. Leakey, A. J. Bloom, E. Carlisle, L. H. Dietterich, G.

Fitzgerald, T. Hasegawa, N. M. Holbrook, R. L. Nelson, M. J. Ottman, V. Raboy, H. Sakai, K. A. Sartor, J. Schwartz, S. Seneweera, M. Tausz and Y. Usui, *Nature*, 2014, **510**, 139-142.

4. J. D. Figueroa, T. Fout, S. Plasynski, H. McIlvried and R. D. Srivastava, *Int. J. Greenh. Gas Control*, 2008, **2**, 9-20.
5. R. S. Haszeldine, *Science*, 2009, **325**, 1647-1652.
6. M. E. Boot-Handford, J. C. Abanades, E. J. Anthony, M. J. Blunt, S. Brandani, N. Mac Dowell, J. R. Fernández, M. C. Ferrari, R. Gross, J. P. Hallett, R. S. Haszeldine, P. Heptonstall, A. Lyngfelt, Z. Makuch, E. Mangano, R. T. J. Porter, M. Pourkashanian, G. T. Rochelle, N. Shah, J. G. Yao and P. S. Fennell, *Energy Environ. Sci.*, 2014, **7**, 130-189.
7. M. Kanniche, R. Gros-Bonnivard, P. Jaud, J. Valle-Marcos, J. M. Amann and C. Bouallou, *Appl. Therm. Eng.*, 2010, **30**, 53-62.
8. R. W. Baker, *Ind. Eng. Chem. Res.*, 2002, **41**, 1393-1411.
9. P. Bernardo, E. Drioli and G. Golemme, *Ind. Eng. Chem. Res.*, 2009, **48**, 4638-4663.
10. C. A. Scholes, K. H. Smith, S. E. Kentish and G. W. Stevens, *Int. J. Greenh. Gas Control*, 2010, **4**, 739-755.
11. S. Basu, A. L. Khan, A. Cano-Odena, C. Q. Liu and I. F. J. Vankelecom, *Chem. Soc. Rev.*, 2010, **39**, 750-768.
12. Y. Yampolskii, *Macromolecules*, 2012, **45**, 3298-3311.
13. L. M. Robeson, *J. Membr. Sci.*, 1991, **62**, 165-185.
14. L. M. Robeson, *Journal of Membrane Science*, 2008, **320**, 390-400.
15. M. Tsapatsis, *Science*, 2011, **334**, 767-768.
16. T. S. Chung, L. Y. Jiang, Y. Li and S. Kulprathipanja, *Prog. Polym. Sci.*, 2007, **32**, 483-507.
17. M. A. Aroon, A. F. Ismail, T. Matsuura and M. M. Montazer-Rahmati, *Separation and Purification Technology*, 2010, **75**, 229-242.
18. G. X. Dong, H. Y. Li and V. Chen, *J. Mater. Chem. A*, 2013, **1**, 4610-4630.
19. V. T. Hoang and S. Kaliaguine, *Chem. Rev.*, 2013, **113**, 4980-5028.
20. M. Rezakazemi, A. E. Amooghin, M. M. Montazer-Rahmati, A. F. Ismail and T. Matsuura, *Prog. Polym. Sci.*, 2014, **39**, 817-861.
21. J. A. Sheffel and M. Tsapatsis, *J. Membr. Sci.*, 2007, **295**, 50-70.
22. C. Rubio, B. Zornoza, P. Gorgojo, C. Téllez and J. Coronas, *Curr. Org. Chem.*, 2014, **18**, 2351-2363.
23. G. Choudalakis and A. D. Gotsis, *Eur. Polym. J.*, 2009, **45**, 967-984.
24. H. K. Jeong, W. Krych, H. Ramanan, S. Nair, E. Marand and M. Tsapatsis, *Chem. Mat.*, 2004, **16**, 3838-3845.
25. A. Galve, D. Sieffert, E. Vispe, C. Tellez, J. Coronas and C. Staudt, *J. Membr. Sci.*, 2011, **370**, 131-140.
26. J. Choi and M. Tsapatsis, *J. Am. Chem. Soc.*, 2010, **132**, 448-449.
27. K. Varoon, X. Y. Zhang, B. Elyassi, D. D. Brewer, M. Gettel, S. Kumar, J. A. Lee, S. Maheshwari, A. Mittal, C. Y. Sung, M. Cococcioni, L. F. Francis, A. V. McCormick, K. A. Mkhoyan and M. Tsapatsis, *Science*, 2011, **334**, 72-75.
28. M. Tsapatsis, *AIChE J.*, 2014, **60**, 2374-2381.
29. W. J. Roth, P. Nachtigall, R. E. Morris and J. Čejka, *Chem. Rev.*, 2014, **114**, 4807-4837.
30. D. Zhao, D. Q. Yuan and H. C. Zhou, *Energy Environ. Sci.*, 2008, **1**, 222-235.
31. M. P. Suh, H. J. Park, T. K. Prasad and D. W. Lim, *Chem. Rev.*, 2012, **112**, 782-835.
32. J. R. Li, J. Sculley and H. C. Zhou, *Chem. Rev.*, 2012, **112**, 869-932.
33. K. Sumida, D. L. Rogow, J. A. Mason, T. M. McDonald, E. D. Bloch, Z. R. Herm, T. H. Bae and J. R. Long, *Chem. Rev.*, 2012, **112**, 724-781.
34. S. L. Qiu, M. Xue and G. S. Zhu, *Chem. Soc. Rev.*, 2014, **43**, 6116-6140.
35. M. Shah, M. C. McCarthy, S. Sachdeva, A. K. Lee and H. K. Jeong, *Ind. Eng. Chem. Res.*, 2012, **51**, 2179-2199.
36. J. Lee, O. K. Farha, J. Roberts, K. A. Scheidt, S. T. Nguyen and J. T. Hupp, *Chem. Soc. Rev.*, 2009, **38**, 1450-1459.
37. A. Corma, H. Garcia and F. X. L. Xamena, *Chem. Rev.*, 2010, **110**, 4606-4655.
38. Y. J. Cui, Y. F. Yue, G. D. Qian and B. L. Chen, *Chem. Rev.*, 2012, **112**, 1126-1162.
39. M. Zhang, G. X. Feng, Z. G. Song, Y. P. Zhou, H. Y. Chao, D. Q. Yuan, T. T. Y. Tan, Z. G. Guo, Z. G. Hu, B. Z. Tang, B. Liu and D. Zhao, *J. Am. Chem. Soc.*, 2014, **136**, 7241-7244.
40. H. B. T. Jeazet, C. Staudt and C. Janiak, *Dalton Trans.*, 2012, **41**, 14003-14027.
41. I. Erucar, G. Yilmaz and S. Keskin, *Chem.-Asian J.*, 2013, **8**, 1692-1704.
42. B. Zornoza, C. Tellez, J. Coronas, J. Gascon and F. Kapteijn, *Microporous Mesoporous Mat.*, 2013, **166**, 67-78.
43. B. Seoane, J. Coronas, I. Gascon, M. E. Benavides, O. Karvan, J. Caro, F. Kapteijn and J. Gascon, *Chem. Soc. Rev.*, 2015, **44**, 2421-2454.
44. T. X. Yang, Y. C. Xiao and T. S. Chung, *Energy Environ. Sci.*, 2011, **4**, 4171-4180.
45. T. X. Yang, G. M. Shi and T. S. Chung, *Adv. Energy Mater.*, 2012, **2**, 1358-1367.
46. T. H. Bae, J. S. Lee, W. L. Qiu, W. J. Koros, C. W. Jones and S. Nair, *Angew. Chem. Int. Ed.*, 2010, **49**, 9863-9866.
47. S. Keskin and D. S. Sholl, *Energy Environ. Sci.*, 2010, **3**, 343-351.
48. C. Zhang, Y. Dai, J. R. Johnson, O. Karvan and W. J. Koros, *J. Membr. Sci.*, 2012, **389**, 34-42.
49. C. Zhang, K. Zhang, L. R. Xu, Y. Labreche, B. Kraftschik and W. J. Koros, *AIChE J.*, 2014, **60**, 2625-2635.
50. T. Rodenas, I. Luz, G. Prieto, B. Seoane, H. Miro, A. Corma, F. Kapteijn, F. X. L. I. Xamena and J. Gascon, *Nat. Mater.*, 2015, **14**, 48-55.
51. N. Stock and S. Biswas, *Chem. Rev.*, 2012, **112**, 933-969.
52. V. Valtchev and L. Tosheva, *Chem. Rev.*, 2013, **113**, 6734-6760.
53. P. Amo-Ochoa, L. Welte, R. González-Prieto, P. J. S. Miguel, C. J. Gómez-García, E. Mateo-Martí, S. Delgado, J. Gómez-Herrero and F. Zamora, *Chem. Commun.*, 2010, **46**, 3262-3264.
54. P. Z. Li, Y. Maeda and Q. Xu, *Chem. Commun.*, 2011, **47**, 8436-8438.
55. P. J. Saines, J. C. Tan, H. H. M. Yeung, P. T. Barton and A. K. Cheetham, *Dalton Trans.*, 2012, **41**, 8585-8593.
56. J. C. Tan, P. J. Saines, E. G. Bithell and A. K. Cheetham, *ACS Nano*, 2012, **6**, 615-621.
57. A. Gallego, C. Hermosa, O. Castillo, I. Berlanga, C. J. Gómez-García, E. Mateo-Martí, J. I. Martínez, F. Flores, C. Gómez-Navarro, J. Gómez-Herrero, S. Delgado and F. Zamora, *Adv. Mater.*, 2013, **25**, 2141-2146.

58. T. Araki, A. Kondo and K. Maeda, *Chem. Commun.*, 2013, **49**, 552-554.
59. Y. Peng, Y. S. Li, Y. J. Ban, H. Jin, W. M. Jiao, X. L. Liu and W. S. Yang, *Science*, 2014, **346**, 1356-1359.
60. M. Hu, S. Ishihara and Y. Yamauchi, *Angew. Chem. Int. Ed.*, 2013, **52**, 1235-1239.
61. S. Motoyama, R. Makiura, O. Sakata and H. Kitagawa, *J. Am. Chem. Soc.*, 2011, **133**, 5640-5643.
62. T. Tsuruoka, S. Furukawa, Y. Takashima, K. Yoshida, S. Isoda and S. Kitagawa, *Angew. Chem. Int. Ed.*, 2009, **48**, 4739-4743.
63. M. H. Pham, G. T. Vuong, F. G. Fontaine and T. O. Do, *Cryst. Growth Des.*, 2012, **12**, 3091-3095.
64. T. Uemura, Y. Ono, K. Kitagawa and S. Kitagawa, *Macromolecules*, 2008, **41**, 87-94.
65. W. H. Lin, R. H. Vora and T. S. Chung, *J. Polym. Sci. Pt. B-Polym. Phys.*, 2000, **38**, 2703-2713.
66. S. Horike, R. Matsuda, D. Tanaka, S. Matsubara, M. Mizuno, K. Endo and S. Kitagawa, *Angew. Chem. Int. Ed.*, 2006, **45**, 7226-7230.
67. S. L. Gould, D. Tranchemontagne, O. M. Yaghi and M. A. Garcia-Garibay, *J. Am. Chem. Soc.*, 2008, **130**, 3246-3247.
68. D. I. Kolokolov, H. Jobic, A. G. Stepanov, V. Guillerm, T. Devic, C. Serre and G. Férey, *Angew. Chem. Int. Ed.*, 2010, **49**, 4791-4794.
69. K. S. W. Sing, D. H. Everett, R. A. W. Haul, L. Moscou, R. A. Pierotti, J. Rouquérol and T. Siemieniewska, *Pure Appl. Chem.*, 1985, **57**, 603-619.
70. Z. G. Hu, K. Zhang, M. Zhang, Z. G. Guo, J. W. Jiang and D. Zhao, *ChemSusChem*, 2014, **7**, 2791-2795.
71. A. L. Myers and J. M. Prausnitz, *AICHE J.*, 1965, **11**, 121-127.
72. N. F. Cessford, N. A. Seaton and T. Düren, *Ind. Eng. Chem. Res.*, 2012, **51**, 4911-4921.
73. D. R. Pesiri, B. Jorgensen and R. C. Dye, *J. Membr. Sci.*, 2003, **218**, 11-18.
74. R. Mahajan, R. Burns, M. Schaeffer and W. J. Koros, *J. Appl. Polym. Sci.*, 2002, **86**, 881-890.
75. T. T. Moore and W. J. Koros, *Journal of Molecular Structure*, 2005, **739**, 87-98.
76. E. V. Perez, K. J. Balkus, J. P. Ferraris and I. H. Musselman, *J. Membr. Sci.*, 2009, **328**, 165-173.
77. S. W. Rutherford and D. D. Do, *Adsorpt.-J. Int. Adsorpt. Soc.*, 1997, **3**, 283-312.
78. W. J. Koros and G. K. Fleming, *J. Membr. Sci.*, 1993, **83**, 1-80.
79. W. R. Vieth, J. M. Howell and J. H. Hsieh, *J. Membr. Sci.*, 1976, **1**, 177-220.
80. A. Bos, I. G. M. Pünt, M. Wessling and H. Strathmann, *J. Membr. Sci.*, 1999, **155**, 67-78.
81. L. L. Zhang, Z. Q. Hu and J. W. Jiang, *J. Phys. Chem. C*, 2012, **116**, 19268-19277.
82. L. Ge, W. Zhou, V. Rudolph and Z. H. Zhu, *J. Mater. Chem. A*, 2013, **1**, 6350-6358.

Mixed Matrix Membranes Comprising Two-Dimensional Metal-Organic Framework Nanosheets for Pre-Combustion CO_2 Capture: A Relationship Study of Filler Morphology versus Membrane Performance

Zixi Kang, Yongwu Peng, Zhigang Hu, Yuhong Qian, Chenglong Chi, Ling Yong Yeo, Lincoln Tee, and Dan Zhao*

Department of Chemical and Biomolecular Engineering, National University of Singapore, 4 Engineering Drive 4, 117585, Singapore
**E-mail: chezhao@nus.edu.sg*

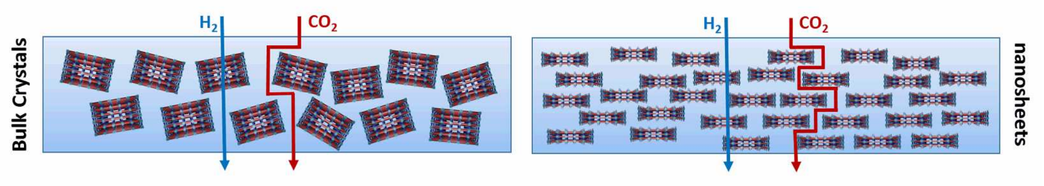

Mixed matrix membranes (MMMs) containing metal-organic frameworks (MOFs) in the morphologies of bulk crystal, nanocube, and nanosheet have been fabricated and their performance in pre-combustion CO_2 capture (H_2/CO_2 separation) has been evaluated. The nanosheet MOFs exhibit partially oriented stacking in polymer matrix, leading to increased H_2 permeability and H_2/CO_2 selectivity that exceed the 2008 Robeson upper bound.